Journal of Contaminant Hydrology 220 (2019) 108–118

Contents lists available at ScienceDirect

Journal of Contaminant Hydrology

journal homepage: www.elsevier.com/locate/jconhyd

Transport of oxygen into granitic rocks: Role of physical and mineralogical heterogeneity

Paolo Trinchero[a,*], Magnus Sidborn[b], Ignasi Puigdomenech[c], Urban Svensson[d], Hedieh Ebrahimi[a], Jorge Molinero[a], Björn Gylling[e], Dirk Bosbach[f], Guido Deissmann[f]

[a] AMPHOS 21 Consulting S.L., Carrer de Veneçuela, 103, 08019 Barcelona, Spain
[b] Kemakta, Box 12655, 112 93 Stockholm, Sweden
[c] Swedish Nuclear Fuel and Waste Management Company, Box 3091, SE-169 03 Solna, Sweden
[d] Computer-Aided Fluid Engineering AB, Frankes väg 3, 371 65 Lyckeby, Sweden
[e] Gylling GeoSolutions, 3556 Davis Street, Evanston, IL 60203, USA
[f] Institute for Energy and Climate Research: Nuclear Waste Management and Reactor Safety (IEK-6) and JARA-HPC, Forschungszentrum Jülich GmbH, 52425 Jülich, Germany

ARTICLE INFO

Keywords:
Oxygen transport
Mineralogical heterogeneity
micro-DFN
High performance computing

ABSTRACT

The rock matrix of granites is expected to be an important buffer against the dispersion of contaminants, *e.g.* radionuclides, and against the ingress of oxygenated glacial meltwater. The influence of matrix heterogeneity on O_2 diffusive transport is assessed here by means of numerical experiments based on a micro-Discrete Fracture Network (micro-DFN) representation of the diffusion-available pore space along with random realisations of idealized biotite grains, to simulate the heterogeneous nature of granitic rocks. A homogeneous-based analytical solution is also presented and used to assess possible deviations of the numerical experiments from the assumption of homogeneity. The analytical solution is also used to test upscaled values of mineral surface area. The numerical experiments show that the matrix behaves as a composite system, with the coexistence of fast and slow diffusive pathways. This behavior is more evident at low Damköhler numbers. Our interpretation of the numerical experiments points out the importance to properly characterise the heterogeneity of the rock matrix.

1. Introduction

Granitic rocks and other crystalline rocks are under consideration by different countries as an option for hosting deep geological repositories for spent nuclear fuel. Some of these repositories will possibly be built at moderate to high latitudes, which makes the question relevant of how a glacier terminus laying above the repository location could affect the hydrogeological and hydrogeochemical conditions at repository depth.

One of the possible effects is that O_2-rich glacial meltwater, driven by the high hydrological gradients expected during a glacial cycle (Vidstrand et al., 2013, 2014), could infiltrate deep into the geological system. Understanding the buffering capacity of the host rock is then important to evaluate whether the redox perturbation may reach repository depth and *e.g.* induce canister corrosion as well as enhance radionuclide mobility (Banwart et al., 1999).

Although microbes are diligent in metabolizing organic matter with oxygen, the expected low concentrations of organic carbon in subglacial environments implies that microbial processes can not be relied on when evaluating the fate of oxygen in glacial meltwaters infiltrating deeply into the ground. The main abiotic processes involved in the depletion of dissolved oxygen (*i.e.* the oxidation of dissolved Fe^{2+} and of Fe(II)-bearing minerals) have been included in a number of homogeneous-based analytical (Sidborn and Neretnieks, 2007; Sidborn et al., 2010; Antonellini et al., 2017) and numerical (Glynn et al., 1999; Auqué et al., 2006; Guimerà et al., 2006; Spiessl et al., 2008, 2009; MacQuarrie et al., 2010) models. In these models, heterogeneity due to *e.g.* the sparse distribution of geochemically reactive minerals, is assessed by means of sensitivity analyses where specific parameters (*e.g.* the mineral surface area or the mineral volume fraction) are varied over plausible ranges.

An explicit analysis of the combined role of physical and mineralogical heterogeneity on the buffering capacity of fractured crystalline rocks has been carried out in two recent articles by Trinchero et al. (2017, 2018). However, these studies focused on the role of fracture coating minerals. Here, we assess how rock matrix heterogeneity affects

* Corresponding author.
E-mail address: paolo.trinchero@amphos21.com (P. Trinchero).

https://doi.org/10.1016/j.jconhyd.2018.12.001
Received 29 November 2018; Accepted 5 December 2018
Available online 07 December 2018

the buffering capacity of a granitic rock. We also evaluate how small-scale heterogeneity can be upscaled by means of an equivalent mineral surface area approach.

2. Problem statement

2.1. The heterogeneous nature of granitic rocks

Granitic rocks are heterogeneous at several scales. At the regional and repository site scale, several rock units with different types of granitic and crystalline rocks are generally found, as seen in the examples of Olkiluoto (Posiva, 2013) and Forsmark (Andersson et al., 2013) (the prospective sites for spent nuclear fuel repositories in Finland and Sweden, respectively). In the context of the diffusive transport of reactive solutes, two types of heterogeneity are important: "physical heterogeneity", which is related to the distribution of the diffusion-available pore space, and "mineralogical heterogeneity", which refers to sparse distribution of the different mineral types and their respective size variability.

Physical heterogeneity of granitic and crystalline rocks is generally evident from micro-scale analyses. For instance, Fig. 1 shows the autoradiograph of a granodiorite sample (Widestrand et al., 2010) from the Äspö Hard Rock Laboratory at Oskarshamn, Sweden, impregnated with 14C-PMMA (polymethylmethacrylate). The dark areas in the autoradiograph indicate connected porosity. Sammaljärvi et al. (2017) describe the pore space in crystalline rocks as the sum of micro-fractures, inter-granular grain boundary pores, which surround mineral grains, and the intra-granular porosity found within mineral grains. Despite the complexity of the structure of the pore space, Svensson et al. (2018) have recently shown that it can be fairly well approximated by a micro-Discrete Fracture Network (micro-DFN).

Besides the pore-space, the different mineral grains are also heterogeneously distributed, in a random manner in granites, but foliated distributions are observed in gneissic rocks. In the context of granitic rock, a particularly interesting mineral phase is biotite ($K(Mg,Fe)_3A1Si_3O_{10}(OH)_2$), an iron(II)-bearing mineral that has the potential to retain potentially harmful dissolved radionuclides (Kyllönen et al., 2014) and that can also reduce and buffer the ingress of O_2-rich waters (Sidborn and Neretnieks, 2007; Malmström and Banwart, 1997). As exemplified by the photograph shown in Fig. 1, biotite grains are dispersed in a random manner in Äspö granodiorite. Observations made with microscopy in a granitic rock sample taken at Forsmark, Sweden, suggest that typical biotite grains there have an average size of $\sim 400 \times 200\,\mu m^2$ ($0.08\,mm^2$) although aggregates of grains up to $2\,mm^2$ can also be found (Drake et al., 2006).

The influence of the physical and mineralogical heterogeneity of the rock matrix on buffering mechanisms against oxygen diffusive penetration is studied in this paper. The investigation is carried out using a micro-DFN model combined with random distributions of mineral grains. An analytical solution is first introduced, which is used to interpret the results of the numerical experiments as well as to evaluate upscaled parameters of mineral surface area.

2.2. Oxygen transport and abiotic buffering mechanisms

We consider a hydraulically active fracture with a continuous recharge of oxygenated water at the upstream boundary. Oxygen in the fracture diffuses from the fracture into the rock matrix where it is consumed by the dissolution of a Fe(II)-bearing reduced mineral, *i.e.* biotite.

2.2.1. Governing equations

The conceptual model is first solved analytically here. The model is comprised of a dual-porosity domain that includes a fracture where transport is dominated by advection and an adjacent rock matrix where transport is dominated by diffusion. Equations describing the mass-balance of dissolved oxygen, ferrous iron, and biotite are expressed for the rock matrix in Eq. (1) and for the fracture in Eq. (2).

$$\frac{\partial c_1'}{\partial t} - D_p \frac{\partial^2 c_1'}{\partial z^2} = -f R_{ox} \tag{1a}$$

$$\frac{\partial c_2'}{\partial t} - D_p \frac{\partial^2 c_2'}{\partial z^2} = R_{diss} - R_{ox} \tag{1b}$$

$$\frac{\partial c_3'}{\partial t} = -R_{diss} \tag{1c}$$

$$\frac{\partial c_1}{\partial t} - D_w \frac{\partial^2 c_1}{\partial x^2} + v \frac{\partial c_1}{\partial x} = D_e \frac{2}{\delta} \frac{\partial c_1'}{\partial z}\bigg|_{z=0} - f\, R_{ox} \tag{2a}$$

$$\frac{\partial c_2}{\partial t} - D_w \frac{\partial^2 c_2}{\partial x^2} + v \frac{\partial c_2}{\partial x} = D_e \frac{2}{\delta} \frac{\partial c_2'}{\partial z}\bigg|_{z=0} - R_{ox} \tag{2b}$$

where $c_1'(x,z,t)$, $c_2'(x,z,t)$ and $c_3'(x,z,t)$ [mol/L_w] (with subscript w denoting *water*) are, respectively, the matrix pore-water concentrations of O_2, Fe^{2+}, and Fe(II) in biotite expressed based on the volume of pore-water. Concentrations are dependent on the spatial location along the flowing fracture (x), the normal distance from the fracture surface into the rock matrix (z), and vary transiently with time (t). Corresponding concentrations of O_2 and Fe^{2+} in the flowing fracture (*i.e.* at $z = 0$) are denoted without apostrophes. Biotite grains are present in the matrix only. The advective water velocity in the fracture and the fracture aperture width are denoted v [m/s] and δ [m] respectively. D_p [m^2/s], D_w [m^2/s], and D_e [m^2/s] are the pore diffusivity in the rock matrix, diffusivity in the fracture water, and the effective diffusivity in the rock matrix, respectively. The effective diffusion coefficient is defined as $D_e = D_w \cdot \phi/\tau_D^2$ (where ϕ is the diffusion available porosity, and τ_D is the effective tortuosity of the porous medium, see Svensson et al. (2018)), while the pore diffusion coefficient is $D_p = D_e/\phi$, that is, $D_p = D_w/\tau_D^2$. In this model oxygen is consumed abiotically through a serial process involving non-oxidative dissolution of ferrous iron in

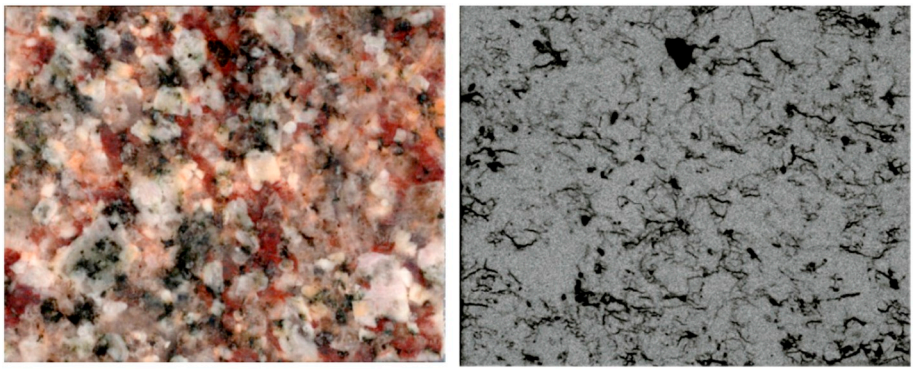

Fig. 1. Left: Photography of an intact porphyritic Ävrö granodiorite sample from Oskarshamn, Sweden, showing biotite (black grains), as well as quartz and feldspar (gray, white and pink grains). Right: 14C-PMMA autoradiograph of the same sample where blackening in the autoradiograph indicates connected pore space. From Widestrand et al. (2010); sample A03:7 from borehole KA3065A03. The width of the sample is 23 mm. (For interpretation of the references to colour in this figure legend, the reader is referred to the web version of this article.)

Table 1
List of parameters for the analytical model.

Parameter	Value	Unit	Comment
c_{20}'	$1.8 \cdot 10^{-6}$	mol/L_w	Assumed ferrous ion concentration at steady state.
c_{OH^-}'	$1.0 \cdot 10^{-6}$	mol/L_w	Hydroxide ion concentration at pH 8.
f	0.25	–	Stoichiometry of oxidation reaction.
k_r	$1.33 \cdot 10^{12}$	$M_{OH}{}^{-2} atm_{O_2}{}^{-1}\ s^{-1}$	Homogeneous reaction rate constant at 25 °C (Stumm and Lee, 1961).
$k_{Fe,\ diss}$	$5.5 \cdot 10^{-13}$	$mol\ m_m{}^{-2}\ s^{-1}$	Heterogeneous dissolution rate constant at pH 8 Malmström and Banwart, 1997).
kH'	$1.3 \cdot 10^{-3}$	$mol_{O_2}\ L_w{}^{-1}\ atm_{O_2}{}^{-1}$	Henry's law constant (Lide and Frederikse, 1995).

biotite, followed by homogeneous oxidation of dissolved ferrous ions by oxygen ($Fe^{2+} + 0.25\,O_2 + 2.5H_2O \rightarrow Fe(OH)_{3(am)} + 2H^+$) with a reaction stoichiometry factor $f = 0.25$ (moles O_2 per mol Fe). The rates of these individual reactions are assumed to be described by the rate expressions in Eq. (3) expressed in terms of the oxidation/dissolution of ferrous iron.

$$R_{ox}\,[\mathrm{mol_{Fe}L_w^{-1}s^{-1}}] = k_r c_1' c_2' c_{\mathrm{OH}}'^{2}/k_H^{\circ} \tag{3a}$$

$$R_{diss}\,[\mathrm{mol_{Fe}L_w^{-1}s^{-1}}] = \frac{k_{\mathrm{Fe},diss} A_s}{1{,}000\phi}\left(\frac{c_3'}{c_{30}'}\right)^{\frac{2}{3}}\left(1 - \frac{c_2'}{c_{20}'}\right) \tag{3b}$$

where ϕ [−] is the matrix porosity, A_s [m^2/m^3] is the initial biotite specific surface area (note that the specific surface area is here expressed relative to the bulk volume) and c_{20}' [mol/L_w] and c_{30}' [mol/L_w] are, respectively, the ferrous ion concentration at steady state and the initial concentration of Fe(II) in biotite in the matrix.

Field observations at the Forsmark (Hallbeck and Pedersen, 2012; Drake et al., 2018) and Olkiluoto (Bomberg et al., 2015) sites show that the iron(II) concentration in deep groundwaters varies in general between $(0.1\,\mathrm{to}\,40) \cdot 10^{-6}$ mol/L_w. A value $c_{20}' = 1.8 \cdot 10^{-6}$ mol/L_w is used in the calculations hereafter.

The other parameters of Eq. (3) are specified in Table 1, except for the values of A_s, c_{10}, ϕ and D_p, which are case-specific.

2.2.2. Oxidation limited by reactions kinetics

Initially, when the biotite in the rock matrix is unaltered, *i.e.* the ferrous content in biotite is $c_3' \approx c_{30}'$, the overall reaction rate is controlled by dissolution or oxidation reaction kinetics rather than constrained by diffusive transport. These reactions are assumed to occur serially, with an overall rate determined by the slower of the two reaction steps. The overall rate can then be described by either of the rate expressions ($R_{diss} = R_{ox}$) for the condition:

$$c_2' = c_{20}' \frac{k_2}{k_2 + k_1 c_1'} \tag{4}$$

where $k_1 = (k_r/kH')c_{20}'c_{OH^-}'^{2}$ and $k_2 = k_{Fe,\ diss}A_s/(1{,}000\phi)(c_3'/c_{30}')^{2/3}$. Substituting Eq. (4) in the rate expression R_{ox} (Eq. (3a)), and assuming pseudo-steady-state, which implies that $\partial c_1'/\partial t = 0$, the mass-balance equation for oxygen (Eq. (1)) reduces to:

$$D_p \frac{\partial^2 c_1'}{\partial z^2} = f \frac{c_1' k_1}{1 + c_1' k_1/k_2} \tag{5}$$

The right-hand side of this expression describes a reaction rate that gradually changes from zero-order to first-order with respect to the dissolved oxygen concentration, c_1':

$$\text{For } \frac{k_1}{k_2} c_1' \gg 1 \quad \frac{c_1' k_1}{1 + c_1' k_1/k_2} \approx k_2 \qquad \text{(zero-order kinetics)}$$

$$\text{For } \frac{k_1}{k_2} c_1' = 1 \quad \frac{c_1' k_1}{1 + c_1' k_1/k_2} = 0.5 k_1 c_1' = 0.5 k_2 \qquad \text{(transition)}$$

$$\text{For } \frac{k_1}{k_2} c_1' \ll 1 \quad \frac{c_1' k_1}{1 + c_1' k_1/k_2} \approx k_1 c_1' \qquad \text{(first-order kinetics)}$$

Close to the fracture the oxygen concentration may be sufficiently high for the rate to be zero-order. Deep in the matrix, the oxygen concentration approaches zero, and at some distance z_c from the fracture there is a transition from zero-order to first-order kinetics. The concentration at this distance is $c_1'|_{z=z_c} = k_2/k_1$. The general solution to Eq. (5) can be written:

$$c_1' = \begin{cases} a_1 e^{(z-z_c)\sqrt{\alpha}} + a_2 e^{-(z-z_c)\sqrt{\alpha}}, & \text{for } z \geq z_c \\ \dfrac{\beta}{2} z^2 + a_3 z + a_4, & \text{for } z \leq z_c \end{cases} \tag{6}$$

where $\alpha = fk_1/D_p$ and $\beta = fk_2/D_p$ respectively. Note that α and β/c_1' are dimensionless measures of the relative rates of reaction and diffusive transport for the domains of first-order kinetics and zero-order kinetics respectively (commonly referred to as the *second Damköhler numbers*).

The particular solution is derived for the boundary conditions:

$$\begin{aligned} &c_1' = 0 && \text{at } z \to \infty && (\Rightarrow a_1 = 0) \\ &c_1' = k_2/k_1 && \text{at } z = z_c && (\Rightarrow a_2 = k_2/k_1 = \beta/\alpha) \\ &c_1' = c_1 && \text{at } z = 0 && (\Rightarrow a_4 = c_1) \end{aligned} \tag{7}$$

The integration constant a_3 (which can be interpreted as the concentration gradient at the fracture/matrix interface, $(\partial c_1/\partial z)|_{z=0}$) and the distance z_c are finally obtained by assuming that both the concentration and the concentration gradient are continuous at the location of transition $z = z_c$. The concentration of oxygen in the porous rock matrix is then obtained (in Eq. (8)) as a function of α, β, the concentration c_1 of oxygen in the fracture, and the distance into the rock matrix z.

$$c_1' = \begin{cases} \dfrac{\beta}{\alpha} e^{-(z-z_c)\sqrt{\alpha}}, & \text{for } z \geq z_c \\ \dfrac{\beta}{2} z^2 + a_3 z + c_1, & \text{for } z \leq z_c \end{cases} \tag{8}$$

where $z_c = \sqrt{2c_1/\beta - 1/\alpha} - \sqrt{1/\alpha}$, and $a_3 = -\sqrt{2c_1\beta - \beta^2/\alpha}$.

Eq. (8) has been used to assess the possible penetration of oxygen in the last Swedish safety analysis of the potential nuclear waste repository at Forsmark (Sidborn et al., 2010).

An illustrative result for the O_2 concentration profile as a function of distance in the rock matrix is shown in Fig. 2 for the case of a fracture concentration of oxygen $c_1 = 3 \cdot 10^{-5}$ mol_{O_2}/L_w, a biotite specific surface $A_s = 11{,}000$ m^2m^{-3}, a porosity $\phi = 0.0018$ and a pore diffusivity $D_p = 1.17 \cdot 10^{-11}$ m^2/s (SKB, 2010). Additional parameters are given in Table 1.

2.2.3. Oxidation limited by diffusion resistance

With time, diffusion resistance becomes increasingly important as ferrous iron in biotite close to the fracture is exhausted. At some point, the diffusion of dissolved species in the pores of the matrix becomes slow compared to the dissolution/reaction rates, and the reactive

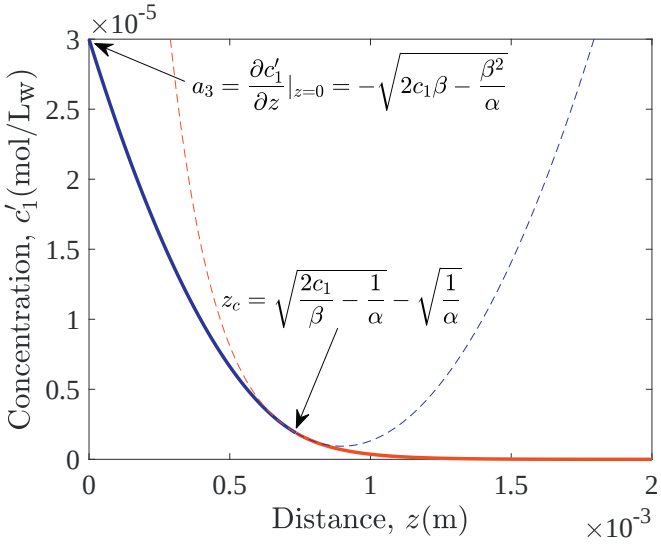

Fig. 2. Illustrative result for a fracture O_2 concentration of $c_1 = 3 \cdot 10^{-5}$ (mol/L_w), a biotite specific surface A_s = 11,000 $m_m{}^2 m_b{}^{-3}$, a porosity $\phi = 0.0018$ and pore diffusivity $D_p = 1.17 \cdot 10^{-11}$ m^2/s SKB (2010). Additional parameters are given in Table 1. Solid curve represents the O_2 concentration profile as a function of distance z in the matrix (see Eq. (8)). Blue solid colour represents domain controlled by zero-order kinetics and red solid colour the domain controlled by first-order kinetics. The concentration gradient at $z = 0$ and the the distance z_c at which the reaction changes from zero-order to first-order kineitcs are indicated. (For interpretation of the references to colour in this figure legend, the reader is referred to the web version of this article.)

process is governed by the diffusion transport resistance. This implies a sharp reaction front that propagates further into the matrix with time. In the fully transient system described by Eq. (1), the dissolution/reaction front propagates into the rock matrix with time coupled with a change in concentration profiles. With the diffusion of dissolved species in the pores of the matrix being fast compared to the front displacement, the concentration profiles are always at steady-state for a certain front location. An analytical solution for this *pseudo-steady-state* is derived in Sidborn and Neretnieks (2007). An equivalent expression was derived by Rajaram and Arshadi (2016) using a similarity solution for reaction front propagation.

2.3. Numerical experiments

The inter-granular space of a synthetic granitic rock is described here using a micro-Discrete Fracture Model (Svensson et al., 2018); *i.e.* three different fracture sets of length from one to a few millimeters are used to mimic grain-boundary pores as well as micro fractures that transect different mineral grains. The micro-DFN, and the equivalent continuous porous medium model based on this micro-DFN, were generated using the finite-volume groundwater flow simulator DarcyTools (Svensson et al., 2010; Svensson and Ferry, 2014). Details on the method to generate the micro-DFN used here is provided in Svensson et al. (2018). The parameters describing each fracture set are listed in Table 2. These parameters are the same used in Svensson et al. (2018) to mimic diffusive properties of a granitic rock sample from borehole KFM02A of Forsmark. However, the numerical grid of this continuum model differs from that of Svensson et al. (2018) in refinement, topology and in the fact that here no cells are deactivated and thus the model should be regarded as synthetic. The properties of the Base Case model, which are discussed in detail in section 3.1, resemble those of a tight granitic rock, with a relatively low amount of exposed mineral surface area.

DFN-derived pore diffusivity and porosity (ϕ[−]) values were assigned to all the active cells of the continuum model using the approach

Table 2
Input data of the micro-DFN.

Parameter	Set 1	Set 2	Set 3
Length interval [mm]	5–20	4–5	1–2
Intensity I [m^{-3}]	0.6	100	500
Aperture [m]	$5 \cdot 10^{-7}$	$5 \cdot 10^{-7}$	$5 \cdot 10^{-7}$
Pore diffusivity D_p [m^2/s]	$4 \cdot 10^{-10}$	$4 \cdot 10^{-10}$	$4 \cdot 10^{-10}$
Power law exponent a	−2.6	−2.6	−2.6
Fracture center	Poisson	Poisson	Close to Set 2
Fracture normal vector orientation	Poisson	Poisosn	Poisson

described by Svensson (2001a, 2001b); *i.e.* intersecting volumes between fractures and grid cells were computed and the contributions from all intersecting fractures were added to the related parameters of each grid cell. The fracture surface (*i.e.* the total fracture surface that intersects a given grid cell, S_F [m^2]) was also retrieved at each grid cell. All the cells that were not in contact with the generated fractures and cells in contact with isolated fractures and their contacting cells were assigned a minimum value of porosity ($\phi = 1 \cdot 10^{-4}$) and pore diffusivity ($D_p = 1.1 \cdot 10^{-15}$ m^2/s).

The resulting distribution of porosity, pore diffusivity and fracture surface is shown in Fig. 3. Note that the bulk pore diffusivity is here obtained by fitting penetration profiles of a conservative tracer, as described in Section 3.1. The bulk porosity of the model is $\overline{\phi} = 2.2 \cdot 10^{-3}$.

The dimension of the continuum model domain is $3.0 \cdot 10^{-2}$ m × $4.75 \cdot 10^{-3}$ m × $1.25 \cdot 10^{-1}$ m and is discretized with

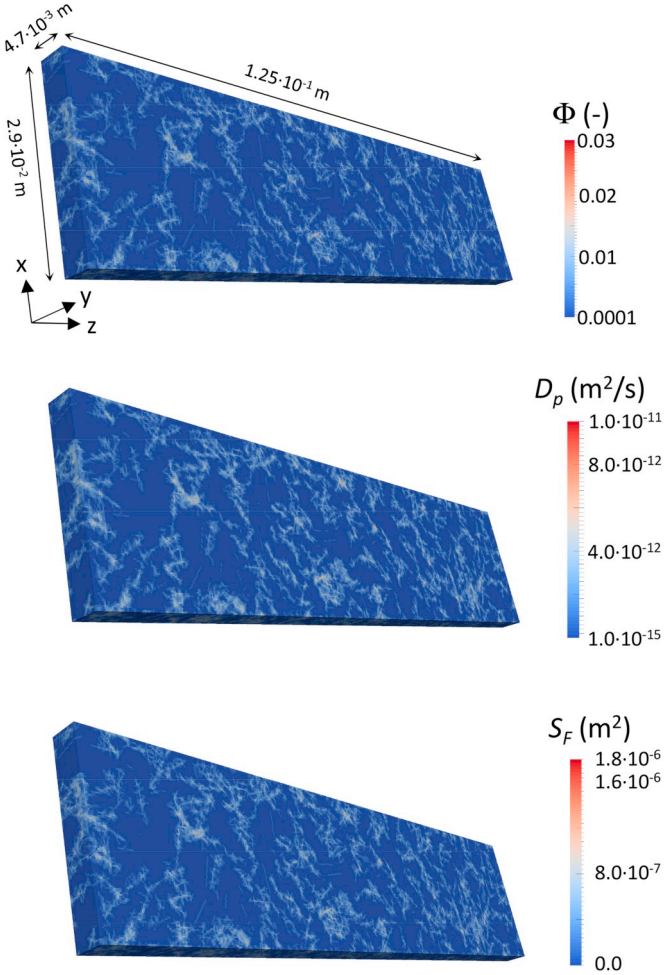

Fig. 3. Distribution of (top) porosity, (middle) pore diffusivity and (bottom) fracture surface in the synthetic rock matrix.

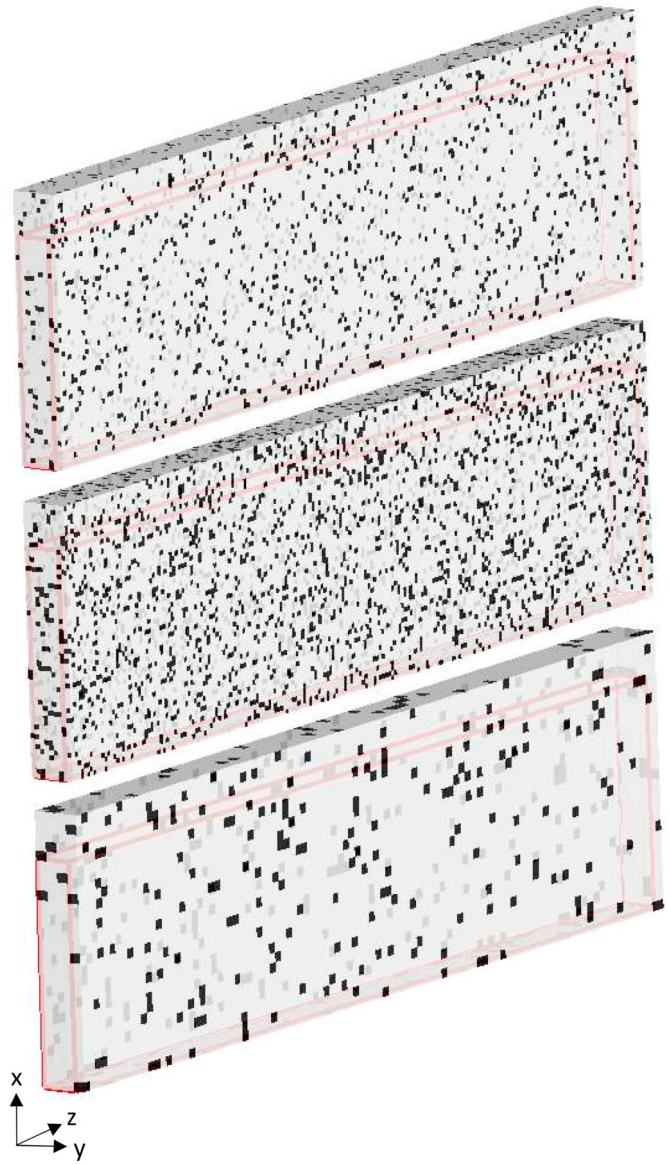

Fig. 4. Top: distribution of biotite grains for both the base case (BC) and variant case 1 (VC1) with higher diffusivity. Middle: the distribution of biotite grains for the variant case 2 (VC2) where the biotite amount is doubled. Bottom: the distribution of biotite grains for the variant case 3 (VC3) where the grain size of the biotite grains is doubled. Black voxels correspond to the biotite grains whereas transparent volumes do not contain biotite. The size of a single dot is equal to δ_{grain} (see Table 3). The red lines show the boundaries of the continuum model. (For interpretation of the references to colour in this figure legend, the reader is referred to the web version of this article.)

$118 \times 19 \times 500 = 1{,}121{,}000$ rectangular cuboids, with constant refinement $\delta_{cont} = 2.5 \cdot 10^{-4} m$.

Biotite grain distributions were generated over an independent grid using binary random uncorrelated realisations that simulate the presence or absence of a biotite grain. The distribution of biotite grains for the different considered cases is shown in Fig. 4 (notice that all the considered cases are discussed in detail further below). The discretization (δ_{grain}) of this "biotite grain grid" coincides with the considered biotite grain size, $6.3 \cdot 10^{-4}$ m.

In the continuum model, mineral dissolution is then parameterised by assuming that for the i-th grid cell the exposed biotite specific surface area is given by:

$$A_{s_i} = \varepsilon_i \cdot S_{F_i} / \delta_{cont}^3 \tag{9}$$

where ε_i is the volume fraction of the cell occupied by biotite.

Each random realisation of biotite is characterised *a-priori* using equivalent values of specific surface area:

$$A_s^{bulk} = \frac{\delta_{cont}^3}{V_b} \sum A_{s_i} \tag{10}$$

where δ_{cont} [m] is the discretisation of the continuum model and V_b is the bulk volume of the rock ($1.75 \cdot 10^{-5}$ m^3).

A_s^{bulk} is the total fracture surface in contact with the reactive mineral (biotite) divided by the bulk volume of the model and it can be directly derived from the underlying DFN.

The system is considered to be initially anoxic and a constant oxygen concentration of $1.5 \cdot 10^{-3}$ mol/L$_w$ (48 mg/L$_w$) is applied at $z = 0$ (the left boundary in Figs. 3 to 6). This value of oxygen concentration was used elsewhere to simulate the ingress of glacial meltwater in a previous work (Trinchero et al., 2017). A conservative tracer is also added to the boundary water. The numerical calculations were carried out using PFLOTRAN (Hammond and Lichtner, 2010), which was run in the supercomputer JUQUEEN of the Jülich Supercomputing Centre (Stephan and Docter, 2015). The geochemical reactions included in PFLOTRAN are those discussed in sub-section 'Oxidation limited by reactions kinetics' and the related parameters are those listed in Table 1, except for the biotite specific surface area that is given by Eq. (9).

Four numerical experiments are considered, a Base Case (BC) and three variant cases, each simulation having a different distribution of biotite and/or different sets of physical parameters (Table 3). In Variant Case 1 (VC1) the pore diffusivity was scaled by multiplying each cell value by a factor of 100, mimicking a more altered granitic rock. In Variant Case 2 (VC2) the average amount of biotite was doubled as compared to the BC, while keeping all other parameters unchanged, and for the Variant Case 3 (VC3) the average size of the biotite grains was increased to approximately the double as compared to the BC (to $1.2 \cdot 10^{-3}$ m, *c.f.* Table 3), with all other parameters kept unchanged. Concerning the amount of biotite used in these models, it is convenient to refer here to the work of Drake et al. (2006), which contains a comprehensive analysis of rock mineralogy at two Swedish sites: Forsmark and Laxemar. In this work, it is reported that the main rock type at the Forsmark site contains biotite in a range of 0.8–8 vol%, while at the Laxemar site the three main rock types (Ävrö granite, quartz monzodiorite and fine-grained dioritoid) contain up to 49 vol% of biotite. Thus, the amount of biotite used in all the numerical experiments described in Table 3 should be considered to represent some of the variability that may be expected in granitic rocks.

3. Results

Snapshots of oxygen concentration at steady state for the four numerical experiments are shown in Fig. 5. For all the experiments, steady state conditions are attained after ~15y, approximately; except for the variant case with higher diffusivity, VC1, where a steady state penetration profile is observed at ~2y, approximately. A summary of the results of the four experiment along with the parameters used to interpret the numerical profiles is provided in Table 4.

3.1. Base case (BC) numerical experiment

The BC numerical experiment was extended in time until a steady state oxygen concentration was observed (~15 yr).

The results are analysed here mostly in terms of penetration profiles, which are computed along 118 different transects (one transect per each grid cell in a row of cells taken at the x-y plane and with $y = 2.4 \cdot 10^{-3} m$) parallel to the z direction (the direction of the oxygen concentration gradient). The x-y location of each transect is the centroid of the corresponding grid cell.

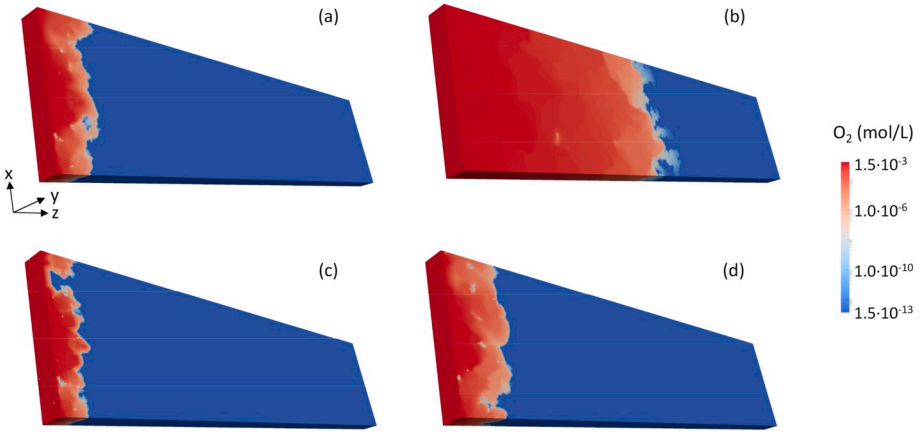

Fig. 5. Concentration of oxygen at steady state for the the (a) BC, (b) VC1, (c) VC2 and (d) VC3 numerical experiments defined in Table 3.

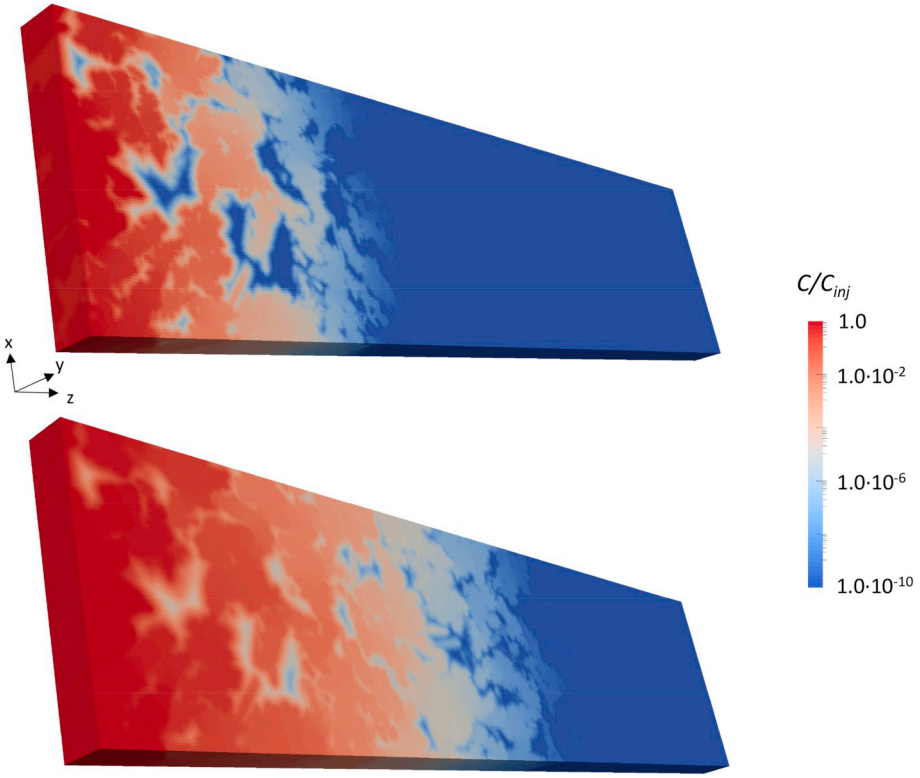

Fig. 6. Normalised tracer concentration at 1.1 yr (top) and 5.1 yr (bottom) for the BC, VC2 and VC3 models (results for VC1 are not shown).

First, the penetration patterns of the conservative tracer (Fig. 6) are analysed in order to infer an equivalent value of pore diffusivity to be used in the subsequent analysis of oxygen transport. The (transient) penetration profiles of the conservative tracer are visually fitted to the analytical solution for diffusion in a plane sheet (Carslaw and Jaeger, 1959; Crank, 1979) (Fig. 7). The best fit is obtained with a value of pore diffusivity of $3.5 \cdot 10^{-13}$ m^2/s. This value, along with the bulk value of porosity is used as input for the analytical solution of oxygen transport.

The computed penetration profiles of oxygen at steady state are shown in Fig. 8a (thin gray lines) along with the average penetration profile (*i.e.* penetration profile obtained with the arithmetic mean of the 118 transects). The analysis of biotite concentration shows that for the considered simulation time frame the consumption of biotite is modest, even close to the injection boundary (results not shown here for the sake of brevity). Thus, the results are interpreted here using the analytical solution provided by Eq. (8) along with the parameters listed in

Table 3
List of numerical experiments with related parameters.

Numerical experiment	Amount of biotite	δ_{grain} [m]	A_s^{bulk} [m^2/m^3]	Other specifications
Base case (BC)	~8%	$6.3 \cdot 10^{-4}$	695	–
Variant case 1 (VC1)	~8%	$6.3 \cdot 10^{-4}$	695	Increased diffusivity
Variant case 2 (VC2)	~16%	$6.3 \cdot 10^{-4}$	1380	–
Variant case 3 (VC3)	~8%	$1.2 \cdot 10^{-3}$	675	–

Table 4
Summary of the results for each of the numerical experiments defined in Table 3, together with the parameters in Eq. (11) used to reproduce the numerical experiments. The last column contains the relative difference (Eq. (13)) between the analytical model (Eq. (8)) and the results from the respective numerical experiment.

Simulation case	A_s^{HR} (m^2/m^3)	f_{HR} [−]	A_s^{HR}/A_s^{LR} [−]	maximum penetration [m]	ξ [−]
Base Case (BC)	320	0.95	2.35	$1.1 \cdot 10^{-2}$	$4.5 \cdot 10^{-1}$
Variant Case 1 (VC1)	600	0.99	1.2	$6.2 \cdot 10^{-2}$	$5.9 \cdot 10^{-2}$
Variant Case 2 (VC2)	400	0.95	2.35	$9.7 \cdot 10^{-3}$	$5.4 \cdot 10^{-1}$
Variant Case 3 (VC3)	252	0.95	2.8	$1.4 \cdot 10^{-2}$	$5.6 \cdot 10^{-1}$

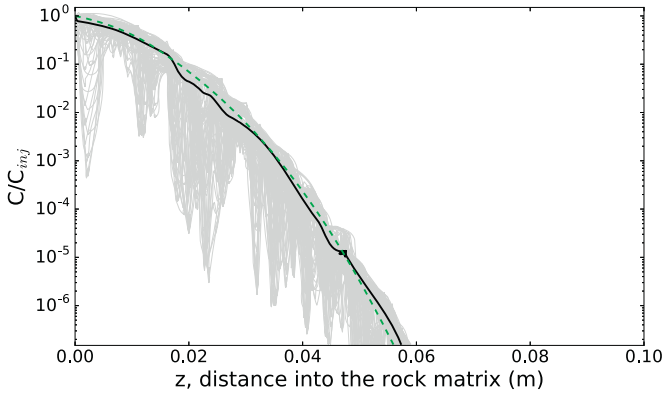

Fig. 7. Penetration profiles of the conservative tracer computed at 5.1 yr along 118 different transects parallel to the z direction (gray lines) for the BC, VC2 and VC3 models (results for VC1 are not shown). The x-y location of each transect corresponds to the centroid of a grid cell. The tracer concentration is normalised by the injection concentration. The thick black line is the average concentration (arithmetic mean) of the 118 profiles. The thick green dashed line is the best fit obtained with the analytical solution Carslaw and Jaeger (1959); Crank (1979). (For interpretation of the references to colour in this figure legend, the reader is referred to the web version of this article.)

Table 1. The same approach has been used for the rest of numerical experiments.

In Fig. 8a, the penetration profile obtained with Eq. (8) using A_s^{bulk} is also shown. This profile significantly overestimates the buffering capacity of the rock (*i.e.* the capacity of the rock to buffer the redox perturbation). The analytical solution is also used to fit the average concentration profiles. Here, the biotite specific surface area is the only fitting parameter and the resulting best-fit value is 320 m^2/m^3. The analytical solution captures well the first part of the profile but deviates from the numerical results at low concentrations.

In Fig. 8b, the analytical solution is used to span all the observed penetration distances (*i.e.* maximum penetration for a given mineral specific surface area). This is done by first computing the two bounding curves (A_s equal to 695 m^2/m^3; *i.e.* shortest penetration and A_s equal to 135 m^2/m^3; *i.e.* longest penetration) and then plotting the other curves with a step size of 5 m^2/m^3. Interestingly, the penetration profile obtained by averaging all these analytically computed curves agrees well with the numerically computed average penetration profile. This indicates that the medium indeed behaves as a composite system, with the average penetration profile being the result of multiple parallel diffusive pathway characterised by different "reactivity".

To further explore this effect, we propose here an alternative simplified analytical model based on two parallel diffusive pathways:

$$c_1' = f_{HR}\, c_1'^{HR} + (1 - f_{HR})\, c_1'^{LR} \tag{11}$$

where f_{HR} is the fraction of oxygen that is driven through the "High Reactive" pathway (superscript HR) and $1 - f_{HR}$ is the remaining part that diffuses along the "Low Reactive" pathway (superscript LR). Both the concentration of oxygen in the high reactive and low reactive pathway ($c_1'^{HR}$ and $c_1'^{LR}$) are calculated using Eq. (8). A similar two-pathways model was used to simulate preferential flow through an unsaturated mining waste rock pile (Trinchero et al., 2011). The influence of the second, less reactive, pathway is visually illustrated in Fig. 9 where oxygen penetration profiles are simulated with arbitrarily selected values and with a range of f_{HR} that spans from 0 to 1. From the figure it is evident that the low reactive pathway, even if present only in a very small fraction, controls the maximum penetration depth of oxygen while f_{HR} controls the transition part of the profile.

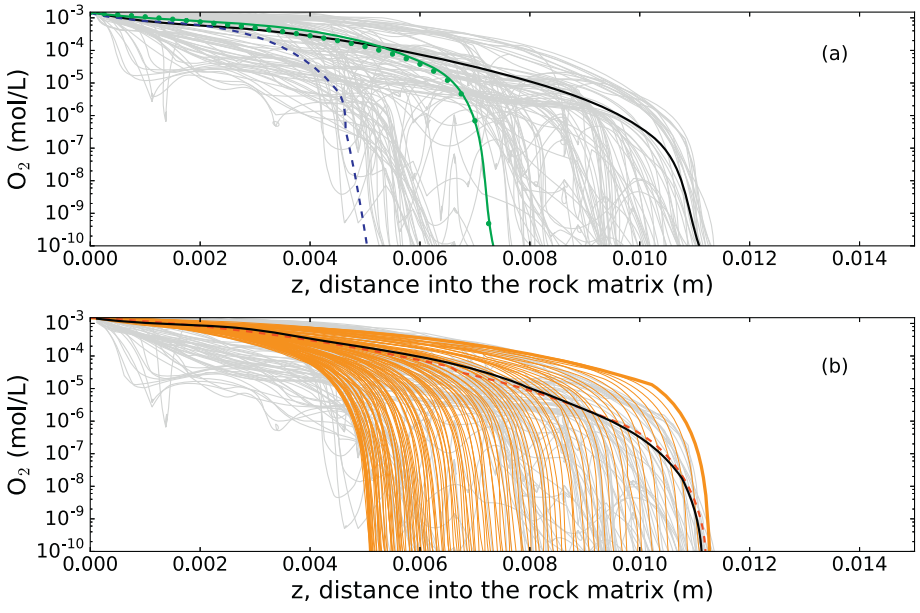

Fig. 8. (a) Oxygen penetration profiles at steady state for the base case (BC) numerical experiment defined in Table 3. The thin gray lines are the oxygen penetration profiles at steady state computed along 118 different transects parallel to the z direction. The x-y location of each transect corresponds to the centroid of a grid cell. The thick black line is the average concentration (arithmetic mean) of the 118 profiles (the same line is used in the bottom figure). The blue dashed line is the oxygen penetration profile obtained with the analytical solution (Eq. (8)) using A_s^{bulk} while the thick continuous dotted green line is the best fit, with $A_s = 320\ m^2/m^3$. In (b) the analytical solution is used to span all the observed penetration distances. The two bounding curves (thick orange lines) are obtained with a value of A_s of 695 m^2/m^3 (shortest penetration) and 135 m^2/m^3 (longest penetration). The thin orange lines are computed using a step size of 5 m^2/m^3 whereas the dashed red line is the average (arithmetic mean) of all the analytically computed profiles. (For interpretation of the references to colour in this figure legend, the reader is referred to the web version of this article.)

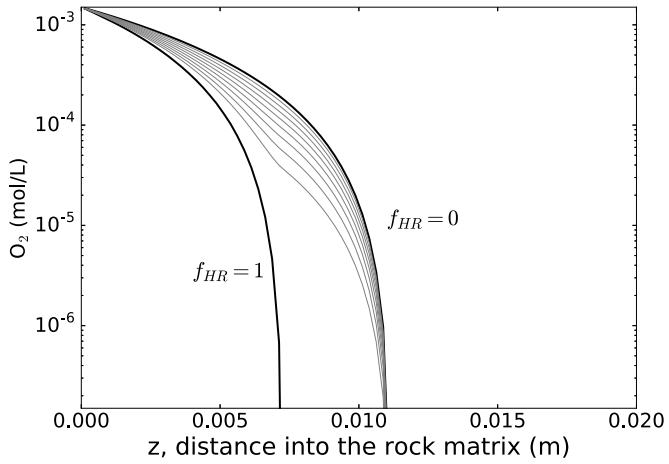

Fig. 9. Illustrative penetration profiles at steady state computed using the two-pathways model, Eq. (11), with arbitrarily selected values. The two thick black lines show the bounding profiles obtained with $f_{HR} = 1.0$ and $f_{HR} = 0.0$. The gray lines are computed with an interval $\Delta f_{HR} = 0.1$.

The two-pathways model (Eq. (11)) was visually fitted to the experimental results, with the following parameters (Table 4) giving a reasonable good match with the experiment (Fig. 10a - thick green dashed line): $f_{HR} = 0.95$, $A_s^{HR} = 320$ m^2/m^3 (*i.e.* same specific surface area used for the single-pathway analytical model, Eq. (8)) and $A_s^{LR} = A_s^{HR}/2.35$.

3.2. VC1 numerical experiment (higher diffusivity)

This variant case tries to mimic a more altered granitic rock by scaling the diffusivity of each cell by a factor of 100. The higher values of diffusivity are close to $1 \cdot 10^{-9}$ m^2/s; *i.e.* the value of molecular diffusion in pure water. The results of this numerical experiment along with the different fits with the analytical solutions are shown in Fig. 10b. For the single pathway analytical model (Fig. 10b - thick green continuous line) the fit was obtained with a value of biotite specific surface area of 600 m^2/m^3. In the two-pathways model (Fig. 10b - thick green dashed line), the same value was used to define A_s^{HR}, whereas f_{HR} was set to 0.99 and $A_s^{LR} = A_s^{HR}/1.2$ (Table 4).

3.3. VC2 numerical experiment (larger amount of biotite)

The results of the VC2 numerical experiment are shown in Fig. 10c. The single pathway analytical model (Eq. (8)) is best fitted to the numerical average profile using a value of specific surface area of 400 m^2/m^3. The two-pathways model (Eq. (11)) is computed by setting A_s^{HR} equal to the value used for the single pathway model, f_{HR} equal to 0.95 and $A_s^{LR} = A_s^{HR}/2.35$.

3.4. VC3 numerical experiment (larger biotite grains)

Fig. 10d shows the penetration profiles of the VC3 numerical experiment. The analytical profile (single pathway model) giving the best fit is computed using a value of specific surface area of 252 m^2/m^3. The two-pathway model (Eq. (11)) is best fitted by setting A_s^{HR} equal to the value used for the single pathway model, f_{HR} equal to 0.95 and $A_s^{LR} = A_s^{HR}/2.8$.

4. Discussion

In safety assessment studies for the geological disposal of spent nuclear fuel, fractured crystalline rock systems are typically conceptualised as dual porosity media with a few hundreds to thousands sparsely distributed fractures and deformation zones that control advective flow patterns and the surrounding "intact rock matrix" being mostly affected by diffusion processes. The "intact rock matrix" is in turn usually described by homogeneous equivalent parameters; *i.e.* pore diffusivity, porosity and, in the presence of geochemical reactions, mineral abundance and surface area (SKB, 2011; Posiva, 2012).

However, there is striking evidence that the "intact rock matrix" is far from being intact as it is characterised by a multi-scale network of micro-fractures, which in turn intersect a complex and heterogeneous distribution of different types of mineral grains (Iraola et al., 2017). Here, we have carried out four numerical experiments focused on assessing the implication of this physical and mineralogical heterogeneous structure on oxygen transport.

For a conservative tracer, the heterogeneous distribution of porosity and pore diffusivity, denoted here as "physical heterogeneity", leads to finger-shaped penetration patterns. However, we have shown that the average penetration profile can be described fairly well by a standard analytical solution based on an equivalent value of diffusivity and porosity.

The results of oxygen concentration are interpreted using a homogeneous-based analytical solution that is presented in the methodological part of this paper. In contrast to the conservative tracer, which is not affected by geochemical reactions and thus is not influenced by "mineralogical heterogeneity", the penetration profiles of oxygen from the micro-DFN based heterogeneous continuum model deviate from those expected when the assumption of homogeneity is invoked. This deviation, which is particularly significant for three out of the four experiments (*i.e.* BC, VC2 and VC3, see Fig. 10), affects the last part of

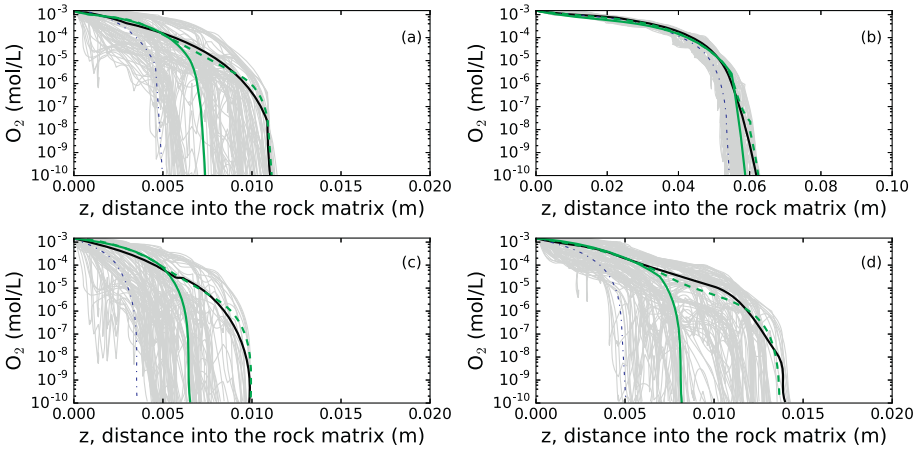

Fig. 10. Oxygen penetration profiles at steady state for the (a) BC, (b) VC1, (c) VC2 and (d) VC3 numerical experiments defined in Table 3. The thin gray lines are the oxygen penetration profiles at steady state computed along the 118 different transects parallel to the *z* direction. The thick black line is the average concentration (arithmetic mean) of the 118 profiles. The blue dash-dotted line is the oxygen penetration profile obtained with the analytical solution (Eq. (8)) using A_s^{bulk}. The thick green lines are the best fit obtained with (continuous line) the analytical solution and (dashed line) the parallel pathways model (Eq. (11)) using the parameters in Table 4. Note that the scale of VC1 is different compared to the other three cases. (For interpretation of the references to colour in this figure legend, the reader is referred to the web version of this article.)

the penetration profiles (*i.e.* low concentration - maximum penetration depth).

The divergence from the homogeneous behavior is interpreted here in terms of an interplay between physical and mineralogical heterogeneity. In particular, in the presence of geochemical reactions and sparsely distributed active grains, the medium behaves as a composite system where a large amount of the oxygen is consumed in highly reactive parts of the domain and a low amount of oxygen can diffuse longer distances along less reactive regions. This effect is quantified using a simplified analytical two-pathway model (Eq. (11)) that gives an estimation of the relative amount between high and low reactive regions (f_{HR}) and the relative "reactivity" between the two regions (the latter is quantified as the ratio between the biotite specific surface area of the high and low reactive region, A_s^{HR}/A_s^{LR}).

In BC, VC2 and VC3 a significant part of the mass of oxygen (~5%; corresponding to $f_{HR} = 0.95$, see Table 4) is shown to diffuse along the less reactive pathway, whose specific surface area is more than twice lower than that of the high reactive system. This composite behavior is less evident for the case with higher diffusivity, VC1, where both f_{HR} and A_s^{HR}/A_s^{LR} are close to unity. This different response is related to the different timescales for diffusion and reactions. The ratio of these timescales is quantified using a global diffusive Damköhler number (D_a), which is however typically employed with n-th order kinetic reactions. Here, we approximate D_a as in Molins et al. (2012):

$$D_a = \frac{1}{1000}\frac{k_{Fe,diss} L}{c'_{20} D_p} \tag{12}$$

where L [m] is the characteristic length for diffusion, which is set here equal to the maximum penetration depth of oxygen ($\sim 1 \cdot 10^{-2}$ m for BC, VC2 and VC3 and $\sim 6 \cdot 10^{-2}$ m for VC1, see Fig. 10). For BC, VC2 and VC3 the Damköhler number is approximately 8.6. This means that in these numerical experiments chemical reactions are dominant over diffusive processes, and this explains the evident signature of heterogeneity in the resulting average profiles seen in Fig. 10. In VC1, with a higher diffusivity, $D_a \sim 0.5$; *i.e.* diffusion becomes dominant and smooths out the irregular mineral distribution thus leading to more homogeneous average profiles. Also, in VC1 a higher value of A_s^{HR} is used (Table 4) as high diffusive processes make more biotite grains available for reactions.

Other interesting results are the influence of biotite abundance and mineral grain size on the extent of oxygen penetration. When a higher amount of biotite is available (VC2 *vs.* BC), the penetration depth of oxygen is slightly lower. However, the system seems to be more sensitive to mineral grain size. In fact, when larger mineral grains are considered (VC3 *vs.* BC), a considerable larger extent of oxygen penetration is observed as a result of the lower equivalent biotite specific surface.

An equivalent value of biotite specific surface has also been tested: A_s^{bulk}, which is the average exposed biotite specific surface area in the whole bulk volume of the rock. In all the considered cases the penetration profiles computed using this equivalent parameter under-estimate the actual oxygen penetration, see Figs. 8 and 10. This underestimation is significant for those cases characterised by a high Damköhler number. On the contrary, for VC1 the equivalent solution provides a reasonable approximation to the results of the numerical experiment, particularly at high oxygen concentrations. This better agreement is due to the importance of diffusion processes for this numerical experiment, which makes more surface area available for reactions.

In a practical application, such as the evaluation of the potential corrosion of a copper canister in a nuclear waste repository, only relatively high oxygen concentrations are of concern. In fact the copper corrosion rate is linearly dependent on oxygen concentration (King et al., 2012). Thus, we evaluate here the relative difference between the analytical solution based on A_s^{bulk} when used to compute the penetration distance for an oxygen concentration of $1 \cdot 10^{-5}$ mol/L (≈0.5 mg/L). The difference (ξ [−]) is calculated as:

$$\xi = \frac{L_{0.5} - L_{0.5}^{bulk}}{L_{0.5}} \tag{13}$$

where $L_{0.5}$ [m] and $L_{0.5}^{bulk}$ [m] are, respectively, the penetration depth computed using the average penetration profile from the related numerical experiment and the analytical solution based on A_s^{bulk}. The results are summarised in the last column of Table 4. For the three cases characterised by a high Damköhler number, the equivalent homogeneous-based solution under-estimates the penetration depth by between 45% and 56%. The under-estimation is slightly higher for the variant case with larger biotite grain sizes, VC3, because the available mineral surface is clustered in bigger grains and, thus, only the external surface is actually exposed to high oxygen fluxes. For low Damköhler numbers (*i.e.* VC1) the deviation is significantly decreased (≈6 %).

A direct comparison of our calculated oxygen penetration depths into the rock matrix with those published in other studies is not straightforward, due to the different parameterisation of the different studies and because none of the previous studies aimed at investigating the role of mineral heterogeneity. The main discrepancies between the parameters for the calculations reported by both Spiessl et al. (2008) and MacQuarrie et al. (2010) as compared with our base case are in the reactive surface area, 66 m^2/m^3 *versus* 695 m^2/m^3, and in the pore diffusivity, $1.1 \cdot 10^{-10}$ m^2/s *versus* $3.5 \cdot 10^{-13}$ m^2/s, and these differences leads, in our calculations, to a shorter penetration of oxygen into the rock matrix. The 1D and 2D calculations reported by Sidborn et al. (2010) showed a good agreement between the analytical expression (Eq. (8)) and their numerical results (Appendix E in Sidborn et al. (2010)). Based on geometrical grain size considerations and a biotite volume fraction of 7.4%, Sidborn et al. (2010) deduced a reactive surface area of 11,100 m^2/m^3, larger than the A_s^{bulk} value obtained from our micro-DFN model (695 m^2/m^3). With this value of reactive surface area, they obtained similar penetration profiles as those computed in the present work for the Base Case simulation. The agreement is due to the fact that the smaller value of surface area used in the Base Case simulation (present work) is counterbalanced by the larger pore diffusivity value used in Sidborn et al. (2010).

Another practical implication that is of high relevance for the safety of a deep geological repository is how the heterogeneous behaviour discussed in this work can affect oxygen advective flow pathways in the surrounding flowing fractures. To discuss this issue we recall that the steady-state oxygen penetration along a flowing fracture depends on the amount of oxygen mass transfer with the surrounding rock matrix (Sidborn et al., 2010). For the same value of effective diffusion, this mass transfer is a function of the interfacial oxygen gradient. For instance, an increased reaction rate (*e.g.* due to a larger equivalent mineral specific surface) implies a steeper interfacial gradient with an increased rate of oxygen mass exchange. When equivalent fluxes computed using the analytical solution based on A_s^{bulk} are compared with the fluxes computed in the four numerical cases, it is found that the homogeneous analytical solution underestimates the average oxygen interfacial flux by a factor between approximately 3 and 4, depending on the numerical case.

5. Conclusions

In fractured crystalline systems, the rock matrix is an important buffer that can *e.g.* retard the migration of radionuclides or consume a part of the oxygen that diffuses from the surface after a glaciation/deglaciation event. In safety analyses of deep geological repositories the rock matrix is typically treated as a secondary continuum with homogeneous physical and mineralogical parameters (SKB, 2011; Posiva,

2012). Here, we have assessed this assumption considering a problem of concern for the afore-mentioned safety analyses: the diffusive penetration of oxygen into an anoxic and initially reducing rock system. Our numerical models have indicated that the combined effect of physical and mineralogical heterogeneity results in oxygen travelling deeper into the rock matrix than estimated by the single pathway homogeneous analytical model.

The evidence of the crystalline rock matrix behaving as a composite system, with the coexistence of fast and slow (or, high reactive and low reactive) diffusive pathways, is consistent with observations made in different laboratory and field experiments (Tsukamoto and Ohe, 1993; Johansson et al., 1998; Nilsson et al., 2010).

Our interpretation of the numerical experiments shows that when assessing the diffusive penetration of oxygen in fractured crystalline systems, the heterogeneity of the rock matrix should be considered. Moreover, a careful characterisation of physical and mineralogical heterogeneity, *e.g.* by means of Scanning Electron Microscopy (SEM) or X-ray Computed Micro-Tomography (X-ray microCT) (Steefel et al., 2015), can provide valuable input for model parameterisation. An equivalent value of specific surface area (A_s^{bulk}; *i.e.* the average exposed mineral specific surface area in the whole bulk volume of the rock) can be used with the analytical solution presented in this paper to provide approximate estimations of the O_2 fluxes into the rock matrix from the groundwaters flowing in fractures.

The analysis presented here has focused on O_2 reactive transport processes in the rock matrix occurring at mm/sub-mm scale in the direction normal to the principal flowpaths along flow-bearing fractures. The extrapolation of these results along the flowpaths to predict the effect of rock matrix heterogeneity on O_2 ingress at to the mesoscale (*e.g.* the scale assessed in *in-situ* experiments (*e.g.* Banwart et al., 1999)) or the site-scale (*i.e.* the scale of interest for safety assessment studies for deep geological disposal) is still an open issue that requires further investigation.

Acknowledgements

PT, MS, US, HE, and JM thank the Swedish Nuclear Fuel and Waste Management Company (SKB) for the financial support. The authors gratefully acknowledge the computing time granted through JARA-HPC on the supercomputer JUQUEEN at Forschungszentrum Jülich.

References

Antonellini, M., Mollema, P., Del Sole, L., 2017. Application of analytical diffusion models to outcrop observations: Implications for mass transport by fluid flow through fractures. Water Resources Research 53, 5545–5566.
Andersson, J., Skagius, K., Winberg, A., Lindborg, T., Ström, A., 2013. Site-descriptive modelling for a final repository for spent nuclear fuel in Sweden. Environ. Earth Sci. 69, 1045–1060.
Auqué, L., Gimeno, M., Gómez, J., Puigdomenech, I., Smellie, J., Tullborg, E., 2006. Groundwater chemistry around a repository for spent nuclear fuel over a glacial cycle. SKB TR-06-31. Svensk Kärnbränslehantering AB, Stockholm, Sweden.
Banwart, S.A., Wikberg, P., Puigdomenech, I., 1999. Protecting the redox stability of a deep repository: Concepts, results and experience from the Äspö hard rock laboratory. In: Metcalfe, R., Rochelle, C.A. (Eds.), Chemical Containment of Waste in the Geosphere. Vol. 157. Geological Society, London, pp. 85–99 Special Publications.
Bomberg, M., Nyyssönen, M., Pitkänen, P., Lehtinen, A., Itävaara, M., 2015. Active microbial communities inhabit sulphate-methane interphase in deep bedrock fracture fluids in Olkiluoto, Finland. BioMed. Res. Int. 2015, ID979530.
Carslaw, H., Jaeger, J., 1959. Conduction of Heat in Solids, 2nd ed. volume 1 Clarendon Press, Oxford.
Crank, J., 1979. The Mathematics of Diffusion. Oxford University Press.
Drake, H., Sandström, B., Tullborg, E., 2006. Mineralogy and Geochemistry of Rocks and Fracture Fillings from Forsmark and Oskarshamn: Compilation of Data for SR-Can. SKB R-06-109. Svensk Kärnbränslehantering AB, Stockholm, Sweden.
Drake, H., Ivarsson, M., Tillberg, M., Whitehouse, M.J., Kooijman, E., 2018. Ancient microbial activity in deep hydraulically conductive fracture zones within the Forsmark target area for geological nuclear waste disposal, Sweden. Geosciences 8, 211.
Glynn, P., Voss, C., Provost, A., 1999. Deep penetration of oxygenated meltwaters from warm based ice sheets into the Fennoscandian shield. In: Use of Hydrogeochemical Information in Testing Groundwater Flow Models. Workshop proceedings, Borgholm, Sweden, 1–3 September 1997. OECD - Nuclear Energy Agency, Paris, France, pp. 201–241.
Guimerà, J., Duro, L., Delos, A., 2006. Changes in Groundwater Composition as a Consequence of Deglaciation. SKB R-06-105. Svensk Kärnbränslehantering AB, Stockholm, Sweden.
Hallbeck, L., Pedersen, K., 2012. Culture-dependent comparison of microbial diversity in deep granitic groundwater from two sites considered for a swedish final repository of spent nuclear fuel. FEMS Microbiol. Ecol. 81, 66–77.
Hammond, G.E., Lichtner, P.C., 2010. Field-scale model for the natural attenuation of uranium at the Hanford 300 area using high-performance computing. Water Resour. Res. 46 (W09527), 1–31.
Iraola, A., Trinchero, P., Voutilainen, M., Gylling, B., Selroos, J.O., Molinero, J., Svensson, U., Bosbach, D., Deissmann, G., 2017. Microtomography-based inter-granular network for the simulation of radionuclide diffusion and sorption in a granitic rock. J. Contam. Hydrol. 207, 8–16.
Johansson, H., Siitari-Kauppi, M., Skålberg, M., Tullborg, E.L., 1998. Diffusion pathways in crystalline rock - examples from Äspö-diorite and fine-grained granite. J. Contam. Hydrol. 35, 41–53.
King, F., Lilja, C., Pedersen, K., Pitkänen, P., Vähänen, M., 2012. An Update of the State-of-the-Art Report on the Corrosion of Copper under Expected Conditions in a Deep Geologic Repository. POSIVA 2011–01. Posiva Oy, Olkiluoto, Eurajoki, Finland.
Kyllönen, J., Hakanen, M., Lindberg, A., Harjula, R., Vehkamäki, M., Lehto, J., 2014. Modeling of cesium sorption on biotite using cation exchange selectivity coefficients. Radiochim. Acta 102, 919–929.
Lide, D.R., Frederikse, H.P.R., 1995. CRC Handbook of Chemistry and Physics, 76th ed. CRC Press, Inc., Boca Raton.
MacQuarrie, K., Mayer, K., Jin, B., Spiessl, S., 2010. The importance of conceptual models in the reactive transport simulation of oxygen ingress in sparsely fractured crystalline rock. J. Contam. Hydrol. 112, 64–76.
Malmström, M., Banwart, S., 1997. Biotite dissolution at 25°C: the pH dependence of dissolution rate and stoichiometry. Geochim. Cosmochim. Acta 61, 2779–2799.
Molins, S., Trebotich, D., Steefel, C.I., Shen, C., 2012. An investigation of the effect of pore scale flow on average geochemical reaction rates using direct numerical simulation. Water Resour. Res. 48 (W03527).
Nilsson, K., Byegård, J., Selnert, E., Widestrand, H., Höglund, S., Gustafsson, E., 2010. Äspö Hard Rock Laboratory. Long Term Sorption Diffusion Experiment (LTDE-SD). Results from rock sample analyses and modelling. SKB R-10-68. Svensk Kärnbränslehantering AB, Stockholm, Sweden.
Posiva, 2012. Safety Case for the Disposal of Spent Nuclear Fuel at Olkiluoto. POSIVA Report 2012-07. Posiva OY, Olkiluoto, Eurajoki, Finland.
Posiva, 2013. Olkiluoto Site Description 2011. POSIVA Report 2011-02. Posiva OY, Olkiluoto, Eurajoki, Finland.
Rajaram, H., Arshadi, M., 2016. A similarity solution for reaction front propagation in a fracture–matrix system. Phil. Trans. R. Soc. A 374, 20150424.
Sammaljärvi, J., Lindberg, A., Voutilainen, M., Ikonen, J., Siitari-Kauppi, M., Pitkänen, P., Koskinen, L., 2017. Multi-scale study of the mineral porosity of veined gneiss and pegmatitic granite from Olkiluoto, Western Finland. J. Radioanal. Nucl. Chem. 314, 1557–1575.
Sidborn, M., Neretnieks, I., 2007. Long term redox evolution in granitic rocks: Modelling the redox front propagation in the rock matrix. Appl. Geochem. 22, 2381–2396.
Sidborn, M., Sandström, B., Tullborg, E.L., Salas, J., Maia, F., Delos, A., Molinero, J., Hallbeck, L., Pedersen, K., 2010. SR-Site: Oxygen Ingress in the Rock at Forsmark During a Glacial Cycle. SKB TR-10-57. Svensk Kärnbränslehantering AB, Stockholm, Sweden.
SKB, 2010. Data Report for the Safety Assessment SR-Site. SKB TR-10-52. Svensk Kärnbränslehantering AB, Stockholm, Sweden.
SKB, 2011. Long-Term Safety for the Final Repository for Spent Nuclear Fuel at Forsmark: Main Report of the SR-Site Project. SKB TR-11-01. Svensk Kärnbränslehantering AB, Stockholm, Sweden.
Spiessl, S., MacQuarrie, K., Mayer, K., 2008. Identification of key parameters controlling dissolved oxygen migration and attenuation in fractured crystalline rocks. J. Contam. Hydrol. 95, 141–153.
Spiessl, S., Mayer, K., MacQuarrie, K., 2009. Reactive Transport Modelling in Fractured Rock - Redox Stability Study. Technical Report NWMO TR-2009-04. Nuclear Waste Management Organization, Toronto, Canada.
Steefel, C.I., Beckingham, L.E., Landrot, G., 2015. Micro-continuum approaches for modeling pore-scale geochemical processes. Rev. Mineral. Geochem. 80, 217–246.
Stephan, M., Docter, J., 2015. JUQUEEN: IBM Blue Gene/Q supercomputer system at the Jülich Supercomputing Centre. J. Large-scale Res. Fac. JLSRF 1.
Stumm, W., Lee, G.F., 1961. Oxygenation of ferrous iron. Ind. Eng. Chem. 53, 143–146.
Svensson, U., 2001a. A continuum representation of fracture networks. Part I: method and basic test cases. J. Hydrol. 250, 170–186.
Svensson, U., 2001b. A continuum representation of fracture networks. Part II: Application to the Äspö Hard Rock laboratory. J. Hydrol. 250, 187–205.
Svensson, U., Ferry, M., 2014. DarcyTools: a computer code for hydrogeological analysis of nuclear waste repositories in fractured rock. J. Appl. Math. Phys. 2, 365.
Svensson, U., Kuylenstierna, H.O., Ferry, M., 2010. DarcyTools Version 3.4: Concepts, Methods and Equations. SKB R-07-38. Svensk Kärnbränslehantering AB, Stockholm, Sweden.
Svensson, U., Löfgren, M., Trinchero, P., Selroos, J.O., 2018. Modelling the diffusion available pore space of an unaltered granitic rock matrix using a micro-DFN approach. J. Hydrol. 559, 182–191.
Trinchero, P., Beckie, R., Sanchez-Vila, X., Nichol, C., 2011. Assessing preferential flow through an unsaturated waste rock pile using spectral analysis. Water Resour. Res. 47, W07532.
Trinchero, P., Puigdomenech, I., Molinero, J., Ebrahimi, H., Gylling, B., Svensson, U., Bosbach, D., Deissmann, G., 2017. Continuum-based DFN-consistent numerical framework for the simulation of oxygen infiltration into fractured crystalline rocks. J. Contam. Hydrol. 200, 60–69.
Trinchero, P., Molinero, J., Ebrahimi, H., Puigdomenech, I., Gylling, B., Svensson, U., Bosbach, D., Deissmann, G., 2018. Simulating oxygen intrusion into highly heterogeneous fractured media using high performance computing. Math. Geosci. 50, 549–567.
Tsukamoto, M., Ohe, T., 1993. Effects of biotite distribution on cesium diffusion in granite.

Chem. Geol. 107, 29–46.
Vidstrand, P., Follin, S., Selroos, J.O., Näslund, J.O., Rhén, I., 2013. Modeling of groundwater flow at depth in crystalline rock beneath a moving ice-sheet margin, exemplified by the Fennoscandian Shield, Sweden. Hydrogeol. J. 21, 239–255.
Vidstrand, P., Follin, S., Selroos, J.O., Näslund, J.O., 2014. Groundwater flow modeling of periods with periglacial and glacial climate conditions for the safety assessment of the proposed high-level nuclear waste repository site at Forsmark, Sweden. Hydrogeol. J. 22, 1251–1267.
Widestrand, H., Byegård, J., Selnert, E., Skålberg, M., Höglund, S., Gustafsson, E., 2010. Long Term Sorption Diffusion Experiment (LTDE-SD). Supporting Laboratory Program – Sorption Diffusion Experiments and Rock Material Characterisation. SKB R-10-66. Svensk Kärnbränslehantering AB, Stockholm, Sweden.